

EXTENDED X-RAY EMISSION FROM QSOS¹

ALAN STOCKTON, HAI FU, AND J. PATRICK HENRY

Institute for Astronomy, University of Hawaii, 2680 Woodlawn Drive, Honolulu, HI 96822

AND

GABRIELA CANALIZO

Department of Physics and Institute of Geophysics and Planetary Physics, University of California, Riverside, CA 95521

accepted for publication in ApJ

ABSTRACT

We report Chandra ACIS observations of the fields of 4 QSOs showing strong extended optical emission-line regions. Two of these show no evidence for significant extended X-ray emission. The remaining two fields, those of 3C 249.1 and 4C 37.43, show discrete (but resolved) X-ray sources at distances ranging from ~ 10 to ~ 40 kpc from the nucleus. In addition, 4C 37.43 also may show a region of diffuse X-ray emission extending out to ~ 65 kpc and centered on the QSO.

It has been suggested that extended emission-line regions such as these may originate in the cooling of a hot intragroup medium. We do not detect a general extended medium in any of our fields, and the upper limits we can place on its presence indicate cooling times of at least a few 10^9 years.

The discrete X-ray emission sources we detect cannot be explained as the X-ray jets frequently seen associated with radio-loud quasars, nor can they be due to electron scattering of nuclear emission. The most plausible explanation is that they result from high-speed shocks from galactic superwinds resulting either from a starburst in the QSO host galaxy or from the activation of the QSO itself. Evidence from densities and velocities found from studies of the extended optical emission around QSOs also supports this interpretation.

Subject headings: quasars: individual (3C 249.1, 4C 25.40, 4C 37.43, Mrk 1014)—X-rays: galaxies

1. INTRODUCTION

A significant fraction of low-redshift QSOs show strong extended emission over radii from the nucleus of a few tens of kiloparsecs or more (Wampler et al. 1975; Stockton 1976; Richstone & Oke 1977; Boroson et al. 1985; Stockton & MacKenty 1987). Briefly, the main features of these extended emission-line regions (EELRs) are that (1) they are often highly structured, with several discrete knots and/or filaments, (2) their morphologies generally do not follow that of either the QSO host galaxy or the radio emission, (3) the inferred ionization parameter indicates that at least some of the emission comes from relatively dense regions (\sim a few hundred cm^{-3}), and (4) the most luminous EELRs are associated with steep spectrum radio-loud QSOs. Currently, the best studied of these EELRs is that of the $z = 0.37$ quasar 4C 37.43 (Stockton et al. 2002), shown in Fig. 1. The origin of the gas comprising these EELRs remains uncertain. Currently, there are three main scenarios:

1. The gas is tidal debris from an interaction or merger, photoionized by UV radiation from the nucleus (Stockton & MacKenty 1987).
2. The gas comes from a cooling flow. The warm gas condenses from hot (10^8 K) gas in a halo surrounding the quasar and is, again, photoionized by the nucleus (Fabian et al. 1987).
3. The gas has been blown out and shocked, either

by a superwind from a vigorous starburst or by a wind generated by the turning on of the QSO (*e.g.*, di Matteo, Springel, & Hernquist 2005). The gas itself may originally have been either tidal debris (as in 1) or simply ambient gas associated with the host galaxy. The gas is photoionized by the UV photons from the nucleus and/or ionized locally by thermal emission from the high-speed shocks propagating through the gas (Stockton et al. 2002).

Crawford, Fabian, and their colleagues have insisted quite strongly that EELRs around QSOs and radio galaxies must have their origins in cooling flows (Fabian et al. 1987; Crawford et al. 1988; Crawford & Fabian 1989; Forbes et al. 1990; Crawford & Vanderriest 2000). They have pointed out that emission regions with the inferred densities will dissipate quite rapidly unless confined by some mechanism, and they suggest that the most reasonable confinement mechanism is a hot external medium. To support this interpretation, they have measured the [O II]/[O III] line ratio and used photoionization models to estimate the ionization parameter and thence the pressure in the EELR. Assuming pressure equilibrium with a hot external medium allows an estimate of the cooling time for the latter. In most cases, this time is found to be much shorter than the Hubble time.

However, there has been no *direct* evidence that cooling flows are important in these cases, and, in any case, the standard cooling-flow paradigm seems to have been ruled out by recent observations (*e.g.*, Peterson et al. 2003). Furthermore, Stockton et al. (2002) have shown from detailed photoionization modeling of the EELR around the quasar 4C 37.43 that at least two density regimes are required, and that these cannot be in pressure equilibrium with each other. This model indicates that a problem with using the [O II]/[O III] line ratio to infer the ionization parameter is that most of the [O II] emis-

¹ Based in part on data obtained with the Chandra X-Ray Observatory, which is operated for the National Aeronautics and Space Administration by the Smithsonian Astrophysical Observatory. Also based in part on observations made with the NASA/ESA Hubble Space Telescope, obtained from the Data Archive at the Space Telescope Science Institute, which is operated by the Association of Universities for Research in Astronomy, Inc., under NASA contract NAS 5-26555.

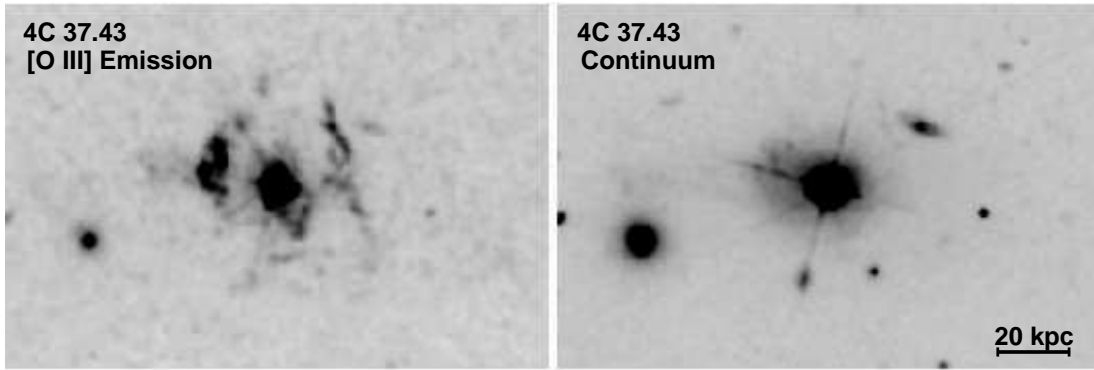


FIG. 1.— HST WFPC2 images of the $z = 0.37$ quasar 4C 37.43. The image on the left is a narrow-band linear-ramp-filter image centered on the [O III] $\lambda 5007$ line. The image on the right is a broad-band F814W image, dominated by continuum light. ($H\alpha$ falling within the edge of this filter profile is responsible for the very weak presence of the strongest emission features). See Stockton et al. 2002 for more details. In this and all following images, north is up and east is to the left.

sion comes from regions with a very small ($\sim 10^{-5}$) filling factor and densities of several hundred cm^{-3} , while almost all of the [O III] emission comes from regions with essentially unity filling factor and densities ~ 200 times lower. The temperatures of these two regions are found to be comparable. The lower-density component could plausibly be in pressure equilibrium with a hot external medium; the denser component cannot be. The confinement mechanism for the dense regions has to be something other than hydrostatic pressure (most likely transient shocks), and the pressure of any hot gas component has to be at least two orders of magnitude lower than that found by Crawford & Vnderriest (2000). The cooling time for such a gas is longer than a Hubble time. This conclusion, of course, depends on whether the best-fitting photoionization model is roughly close to reality; while it was selected from an extensive grid of over 200 model runs, there remain the usual worries about the uniqueness of the solution.

In order to further explore the nature of these EELRs, and, in particular, to test whether a hot gaseous halo of sufficient pressure to have a short cooling time is present, we have obtained deep imaging of three fields with the ACIS on board the Chandra X-ray Observatory. In this paper, we discuss the results of this imaging program, including as well ACIS imaging of one additional QSO EELR field from the Chandra archive. In §2, we describe the observations and reduction procedures. In §3, we discuss the morphologies of the extended X-ray components, comparing them with the optical extended emission. Finally, in §4, we attempt to place these X-ray observations in the overall context of possible models for EELRs. We assume a flat cosmological model with $H_0 = 70 \text{ km s}^{-1}$, $\Omega_m = 0.3$, and $\Omega_\Lambda = 0.7$.

2. OBSERVATIONS, REDUCTION PROCEDURES, AND BASIC RESULTS

Recently, four QSOs having luminous EELRs have been observed with the ACIS onboard the *Chandra* X-ray Observatory (3 from our program no. 04700368 and 1 from program no. 04700768, retrieved from the *Chandra* archive). We give the relevant parameters for these observations in Table 1.

Instead of using the level 2 event files produced by the standard pipeline calibrations, we have gone back to the level 1 event files. The main purpose in doing this was to recover valid source events that were incorrectly rejected as afterglow events by the standard data processing. New level 2 event files were generated after applying the Good Time Intervals (GTIs)

TABLE 1
CHANDRA ACIS OBSERVATIONS OF QSOs WITH EELRS

QSO	Redshift	ACIS CCD	Exposure	Seq No.	Obs ID
MRK 1014	0.159	S3	12 ks	700783	4104
3C 249.1	0.312	I2	24 ks	700665	3986
4C 25.40	0.250	I2	16 ks	700666	3987
4C 37.43	0.371	I2	42 ks	700667	3988

to clean the data of time intervals with high background levels. The data reduction was done with CIAO 3.1 (Chandra Interactive Analysis of Observations)².

We computed model PSFs for each QSO using the Chandra Ray Tracer tool (ChaRT; Carter 2003), which carries out a detailed, frequency-dependent, ray trace of the Chandra optics. We extracted the spectrum of each QSO, using only the grade 0 events (which should be essentially free of pile-up concerns for the flux levels of our sources), and used this model spectrum as input to ChaRT, but with the exposure times increased so that we get roughly the same number of counts as in the “all good grade” images. The simulated distributions of rays were then projected onto the ACIS-I or ACIS-S detector plane, as appropriate, and generated as event files using MARX³.

As explained in §3, we cannot achieve reliable PSF subtraction within $\sim 2''$ radius of the QSOs. Beyond this radius, for two of these fields, those of Mrk 1014 and 4C 25.40, we detect no significant extended component at all. For the remaining two, 4C 37.43 and 3C 249.1, extended emission is observed, but it does not have the character of a hot gaseous halo that would give evidence for a cooling flow. Instead, the X-ray emission appears to be highly structured, and it may to some extent follow the distribution of some of the $\sim 10^4 \text{ K}$ gas producing the extended optical emission. The X-ray emission does not closely follow the radio structure, so this extended component is quite different from the X-ray jets often found around quasars. The remainder of this paper focuses on this extended X-ray emission.

3. THE NATURE OF THE EXTENDED X-RAY EMISSION

² <http://cxc.harvard.edu/ciao/>

³ <http://space.mit.edu/CXC/MARX/>

3.1. The Morphologies of the Extended X-Ray Components

In order to detect and analyze any extended X-ray components, we need to achieve a fairly accurate subtraction of the PSF. For Chandra images, this PSF removal is complicated by two effects: (1) The Chandra PSF is dependent on the X-ray energy, so it is necessary to model the PSF as a weighted sum of mono-energetic PSFs, and (2) regions of high X-ray flux suffer from *pile-up*, such that, if two X-rays fall within the sample time (the default 3.2 s, in our case) and within a 3×3 -pixel detection box, the event may either be rejected or interpreted as a single detection of an X-ray at a higher energy. Pile-up thus results both in loss of counts and in the distortion of the spectral energy distribution. While pile-up should be relatively moderate for our sources, and completely negligible for regions beyond about a $2''$ radius, it could cause problems for our PSF subtraction. We have therefore adopted the following procedure. We extract an image from the level 2 event file over the energy band from 0.5 to 7 keV, using only grade 0 (single pixel) events. These are much less subject to pile-up than are the events of other grades that are normally folded in to make the standard pipeline level-2 image. We model the spectrum of this grade-0 image as a power law combined with photoelectric absorption, and use this model spectrum as the input to ChaRT for producing PSF ray traces. Using MARX, we generate 100 quasi-independent realizations of the PSF and average these to obtain a low-noise PSF. We scale this PSF to the observed level-2 image at a radius of 2 arcsec, where pileup should be negligible, yet the flux is still likely to be dominated by the QSO point source. We then subtract this scaled PSF from the level 2 image, ignoring the region interior to a $2''$ radius, as well as any residuals that clearly are due to slight mismatches between the shapes of the QSO PSF and the synthetic PSF at radii where the profile has a steep gradient.

Figure 2 shows the results of this subtraction for each of the four fields, and Fig. 3 shows the outer parts of the radial-surface-brightness profiles, compared with those of the corresponding scaled synthetic PSFs. We evaluate the significance of apparent features in the difference images from photon statistics based on the counts in the observed images and the scaled PSF models. We discuss the fields individually in the following sections.

3.1.1. Markarian 1014

Markarian 1014 is both the lowest redshift and the only radio-quiet QSO in the sample. It shows the strongest optical extended emission of any of the radio-quiet QSOs in the sample of Stockton & MacKenty (1987), but this emission is still more than a factor of 10 less luminous than the strongest extended emission found in steep-spectrum radio-loud QSOs. The host galaxy is clearly the result of a recent merger: it is an ultraluminous IR source (*e.g.*, Sanders, Scoville, & Soifer 1988), and the optical image shows an enormous, broad, tidal “arm”, with an even larger, much lower surface brightness, counter-arm (*e.g.*, MacKenty & Stockton 1984; Canalizo & Stockton 2000).

The ACIS image shows no significant evidence for extended X-ray emission, either as discrete sources (Fig. 2) or as a diffuse extended component (Fig. 3).

3.1.2. 3C 249.1

The extended optical emission around 3C 249.1 was first noticed spectroscopically by Richstone & Oke (1977) and im-

aged by Stockton & MacKenty (1983, 1987). There appears to be no deep imaging of the host galaxy itself in bands that are not contaminated by the extended emission.

The synthetic PSF is not a perfect match to the actual PSF, as indicated by the large residuals to the NE and SW in the subtracted image (Fig. 2). Nevertheless, there is clear evidence for discrete clumps of X-ray emission to the east and southeast at a radius of about $3''$. There may possibly be some additional clumps to the west at $\sim 15''$ radius, but Fig. 3 shows no evidence for a general diffuse component. A comparison of the ACIS image for 3C 249.1 with optical emission-line images is shown in Fig. 4. The ground-based [O III] image is reproduced from Stockton & MacKenty (1983), and the short-exposure *HST* WFPC2 image was retrieved from the *HST* archive. The brightest detected region of X-ray emission, $3''$ SE of the nucleus (labeled *a*), is nearly coincident with a region of optical emission, seen as a small, arc-like structure in the *HST* image (labeled *a'*). Any X-ray emission coincident with the higher-surface-brightness regions of optical emission closer in would have been swamped by the nuclear X-ray source. There is no detected [O III] emission at the position of the weaker X-ray source *b*. With a proper intensity stretch, both *a* and *b* can be seen clearly on the ACIS images prior to PSF subtraction. Their significance is dominated by photon statistics rather than by any uncertainty in the PSF subtraction. Object *a* is detected at 3σ , while object *b* is detected at just over 2σ .

3.1.3. 4C 25.40

This quasar has a highly structured, filamentary extended emission region in the optical lines (see Fig. 2*j* in Stockton & MacKenty 1987). In our Chandra ACIS image, however, there is no evidence for any significant extended emission either as discrete clumps or as a general surrounding medium.

3.1.4. 4C 37.43

4C 37.43 has the most luminous extended optical emission-line region of any known for low-redshift ($z < 0.5$) QSOs. The host galaxy is clearly detected in both ground-based and *HST* line-free continuum images (Stockton et al. 2002 and references therein; see also Fig. 1); the surface-brightness distribution is asymmetrical, being enhanced towards the east, and there is faint, thin filament extending in the same direction at least 60 kpc from the southern side of the host. The X-ray emission shows several discrete sources at radii ranging from $4''$ to $13''$ (Fig. 5), one of the most luminous being a clump (labeled *d* in Fig. 5, detected at $\sim 4\sigma$) at a radius of about $8''$ (40 kpc, projected) to the east-northeast. This is in the same direction as the strongest optical emission, but at about twice the radius. There is weak optical emission extending out to just south of this position. Other strong clumps of X-ray emission are found to the south, northeast and southwest (labeled *a*, *b*, and *c*, respectively); *a* and *b* have discrete [O III] sources just beyond the X-ray emission. There is no discrete [O III] source associated with *c*, although it falls in a region of low-surface-brightness diffuse emission. Object *a* is detected at just over 3σ ; objects *b* and *c* are each over 2.5σ . Weaker clumps of X-ray emission are found in an slightly elliptical halo, out to about $13''$ radius. These are apparently responsible for the $\sim 2\sigma$ enhancement of the X-ray radial-surface-brightness profile over the PSF model seen between $10''$ and $14''$ in Fig. 3. Beyond $14''$, however, the observed

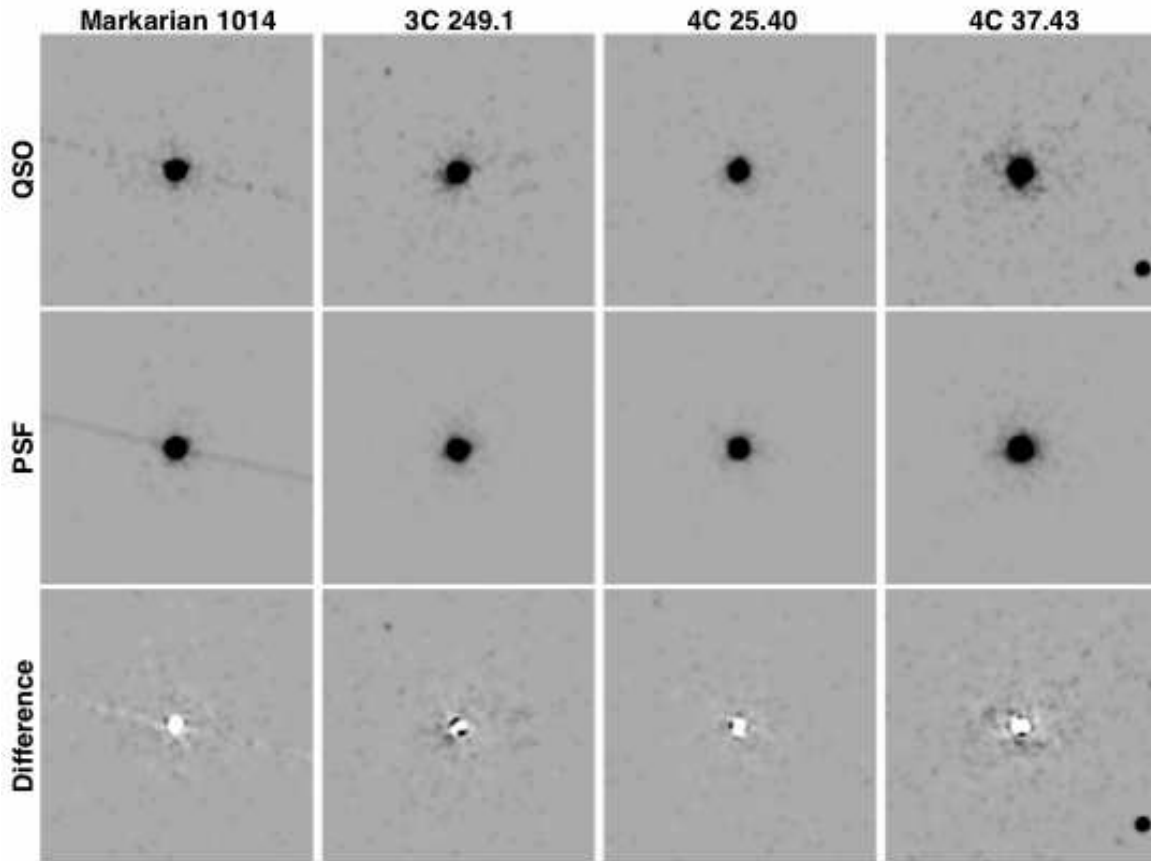


FIG. 2.— Background-subtracted Chandra ACIS images, scaled synthetic PSFs, and differences for the four fields discussed in this paper. All images have been smoothed with Gaussians with $\sigma = 1$ pixel, giving a point-source FWHM of $\sim 1''.8$. The fields shown are $1'$ square. North is up and East to the left.

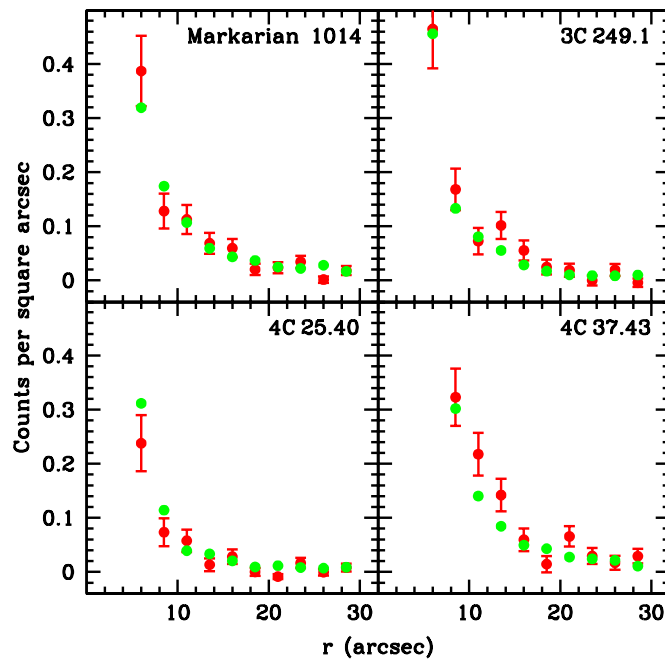


FIG. 3.— Outer X-ray radial-surface-brightness profiles for the targets in our sample (*red*) and our scaled synthetic PSFs (*green*). The random errors for the latter are approximately the size of the points or smaller.

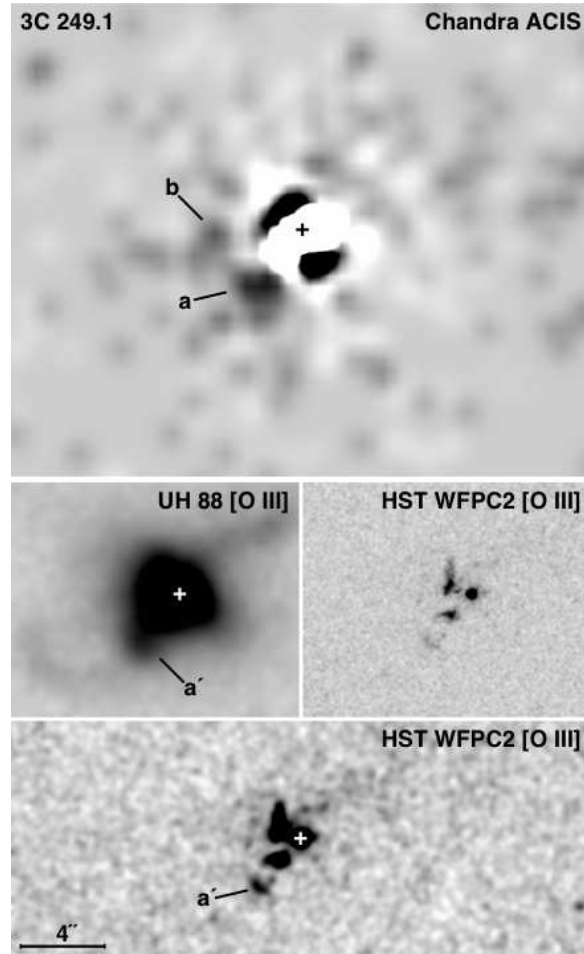


FIG. 4.— Chandra ACIS-I and [O III] images of 3C 249.1. The upper panel shows a higher-contrast version of the difference image from Fig. 2. Two significant regions of off-nuclear X-ray emission are labeled. (Note that, both here and in Fig. 5, the hard stretch and a zero level set just below the sky level tends to overemphasize the negative values just beyond a $2''$ radius, due to the PSF subtraction in regions where there are no X-ray events in the image.) The lower panel shows narrow-band images centered on the redshifted [O III] $\lambda 5007$ emission line. In the upper left of the lower panel is shown a ground-based image of 3C 249.1, taken through a 30 \AA filter (from Stockton & MacKenty 1983; see also Stockton & MacKenty 1987). The remaining two subpanels show, at different contrasts, a [O III] image obtained through the F656N filter with PC1 channel of WFPC2 on *HST*. All images are at the same scale, given in the lower-left corner of the lower panel. Crosses indicate the position of the quasar in cases where this location may be uncertain.

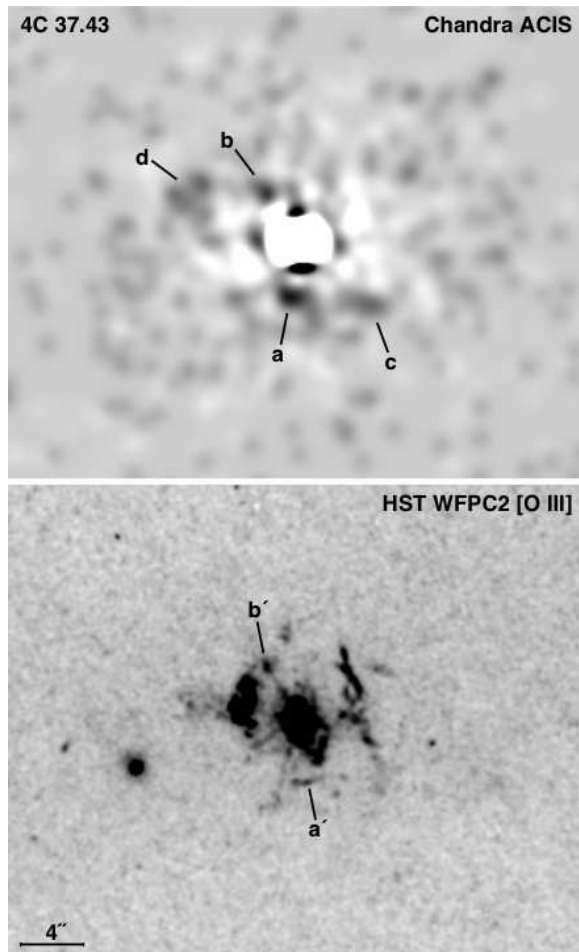


FIG. 5.— Chandra ACIS-I and [O III] images of 4C 37.43. The upper panel shows a higher-contrast version of the difference image from Fig. 2. Several discrete off-nuclear X-ray emission sources are labeled. The lower panel shows a deep *HST* WFPC2 image obtained through a linear ramp filter centered on the redshifted [O III] $\lambda 5007$ emission line (Stockton et al. 2002). The sources labeled a' and b' may be associated with the corresponding X-ray sources. Both images are at the same scale, given in the lower-left corner of the lower panel.

and model PSF profiles are essentially identical, once again indicating the lack of a significant extended X-ray halo component.

3.2. Upper Limits on Extended Diffuse X-Ray Emission

Galaxy groups often show diffuse extended X-ray emission from a hot intragroup medium, indicating the existence of a common potential well sufficiently deep to retain such gas. We have pointed out in our discussions of each of our four fields that we do not see evidence for a diffuse, very extended component. We now need to quantify these statements in terms of upper limits to the presence of such gas. Because of the small numbers of detected events we have to work with, we cannot use constraints from the expected radial surface-brightness profile of the extended component. Instead, we simply deal with counts in a defined annulus, assuming a reasonable model for the distribution of the emission.

We use the annulus from $10''$ to $30''$. A $10''$ inner radius is sufficient to eliminate most of the wings from the QSO PSF, and, at these redshifts, probably most of any diffuse X-ray emission specifically associated with the host galaxy (although, as described below, 4C 37.43 is an exception). The $30''$ outer radius keeps us within a typical group core radius, even for 4C 37.43, the highest redshift object in our sample.

For definiteness, we assume a so-called β (modi-

fied King) model (Cavaliere & Fusco-Femiano 1978; Birkinshaw & Worrall 1993) for the surface brightness distribution:

$$\sigma(r) = \sigma_0 [1 + (r/r_c)^2]^{-3\beta + 0.5},$$

where σ_0 is the central surface brightness and r_c is the core radius. The corresponding density distribution is given by

$$n = n_0 [1 + (r/r_c)^2]^{-3\beta/2}.$$

Basing our choice on the two-component fits to group X-ray emission by Mulchaey & Zabludoff (1998), we assume typical parameters for the extended intragroup medium of $r_c = 175$ kpc, $\beta = 1$, and $kT = 1$ keV. This value for β for the extended component is steeper than that found from single-component fits, which Mulchaey & Zabludoff (1998) found to give unacceptable residuals in most cases.

We determine the counts in the annulus both for the background-subtracted ACIS observations of the four fields and for the corresponding scaled synthetic PSF images. From the photon statistics, we determine the standard deviation of the difference in the annulus, and we take 3 times this value as a conservative upper limit to any contribution from an extended X-ray component. In all cases except the 4C 37.43 field, the difference between the counts in the annulus for the observation and for the synthetic image were $< 1 \sigma$; for 4C 37.43, the counts for the observation are 2σ above those

TABLE 2
UPPER LIMITS TO DIFFUSE EXTENDED EMISSION

QSO	Annular Counts ^a	Model Counts ^b	Luminosity (erg s ⁻¹)	n_{p0} (cm ⁻³)	t_c (Gyr)
MRK 1014	30	92	$< 1.4 \times 10^{43}$	< 0.0014	> 14.2
3C 249.1	25	58	$< 4.2 \times 10^{43}$	< 0.0024	> 8.3
4C 25.40	24	53	$< 3.3 \times 10^{43}$	< 0.0022	> 9.0
4C 37.43	45	76	$< 5.2 \times 10^{43}$	< 0.0027	> 7.4

^aCounts corresponding to 3 times the σ of the difference between the signal in the annulus from $10''$ to $30''$ radius for the background-subtracted Chandra ACIS image and that for the scaled model PSF image.

^bTotal counts within a radius corresponding to $r_c = 175$ kpc for a β model (see text for details) that has been scaled to the counts in column 2 within an annulus from $10''$ to $30''$ radius.

for the PSF model. These extra counts are, however, entirely due to the previously mentioned excess associated with the host. If the inner radius of the annulus is increased from $10''$ to $14''$, the excess in the annulus completely disappears.

From the counts corresponding to the 3σ upper limits in the annulus in each of the fields, we normalize β models with the above parameters at the appropriate redshift. From these models, we calculate the counts we would have expected to receive over the whole circular area out to $10r_c$. After converting to count rates, we then use WebPIMMS⁴ to calculate the corresponding luminosity, assuming a Raymond-Smith model with 0.4-solar metallicity.

In order to obtain a rough upper limit to the central density or pressure, we need the cooling coefficient $L(T)$, where the volume emissivity $\Lambda(T) = L(T)n_en_p$. At $kT = 1$ keV ($T \approx 1.2 \times 10^7$ K), line emission is an important contributor to the cooling. We use the calculation of the cooling coefficient given by Sutherland & Dopita (1993), which gives $L = 1.48 \times 10^{-23}$ erg cm³ s⁻¹. We then integrate the emissivity over the volume out to r_c to find the value of n_{p0} that gives the luminosity found with PIMMS. For these upper limits to the central densities, the lower limits to the cooling times for the gas at the center ranges from $t_c > 7.4 \times 10^9$ years for the 4C 37.43 field to $t_c > 14.2 \times 10^9$ years for the MRK 1014 field. All of the observed and calculated parameters are given in Table 2. While some of the lower limits to the cooling time are formally slightly less than a Hubble time, they do not offer much encouragement to the view that strong cooling is taking place in these groups. Furthermore, as Sutherland & Dopita (1993) stress, these estimates, which assume equilibrium conditions and no effect from the radiation field, will give cooling times considerably lower than those for (more plausible) non-equilibrium models.

4. THE ORIGIN OF THE X-RAY EMISSION

In the two fields for which we detect extended sources of X-ray emission, these sources have distributions similar in extent to those of the extended optical emission. In some cases there may even be correlations between the optical and X-ray brightness peaks; in other cases there clearly is no such correlation. We consider here various possible emission mechanisms for the X-rays.

1. The most common extended X-ray features seen around quasars are X-ray jets (see, e.g., Sambruna et al. 2004;

Marshall et al. 2005, and references therein). These correspond closely in position and morphology to radio jets and are evidently due either to Compton upconversion of microwave background photons by relativistic electrons in the jets or to X-ray synchrotron emission. 3C 249.1 shows a radio jet on the same side as the extended X-ray emission (Miller, Rawlings, & Saunders 1993; Kellerman et al. 1994), but it is at position angle $\sim 99^\circ$, placing it *between* our objects *a* and *b*. While no evidence for a radio jet in 4C 37.43 has yet been detected (Miller, Rawlings, & Saunders 1993), it is a classic FR2 double source, and none of the X-ray emission components lie along the radio axis. In neither case do X-ray jets provide a satisfactory explanation for the observed extended X-ray emission.

2. Some extended X-ray emission in principle might be due to electron scattering of the nuclear X-rays, as has been suggested for some of the near-nuclear soft X-ray emission from the Cygnus A radio galaxy (Young et al. 2002). However, the low Thompson cross-section makes electron scattering an extremely inefficient process, so it is useful to estimate the actual scattered flux in a typical example. While we do not have direct information on the electron densities in the X-ray emitting regions, they are unlikely to be greater than those in the most luminous optical EELRs. We have the required information for the extended emission region about $4''$ east of 4C 37.43. The total mass of the gas in this EELR is $\sim 4 M_\odot$ (Stockton et al. 2002), which gives a total number of electrons of $\sim 10^{57}$, assuming fully ionized pure hydrogen. A typical distance for the X-ray sources is ~ 20 kpc from the nucleus, and we assume that the nuclear X-ray flux in their direction is the same as towards our line of sight. The calculation gives a ratio of scattered to direct nuclear flux of $\sim 10^{-14}$ for a region of typical size. Since, for 4C 37.43, we detect ~ 6700 counts from the nucleus in our 42 ks of integration, we would expect $< 10^{-10}$ counts due to scattering in regions like those we observe. Electron scattering thus fails rather dramatically in this context, even if some of our assumptions were to be incorrect by a few orders of magnitude.
3. In some cases (Sako et al. 2000; Kinkhabwala et al. 2002), the X-ray emission can be dominated by X-ray recombination lines from the $\sim 10^4$ K photoionized gas. Our calculations based on photoionization models for the strongest optical emission region associated with 4C 37.43 (Stockton et al. 2002) indicate that this mechanism could potentially make a significant contribution, but also that there are many uncertainties. The fact that we do not actually detect X-ray emission from any of the most luminous optical extended emission regions in 4C 37.43, nor from any of the extended emission regions of MRK 1014 or 4C 25.40 argues against its importance generally in the cases we are considering.
4. X-ray emission can be thermal emission and line emission from high-speed shocks. The cases where there *may* be a spatial correlation between the optical emission-line gas and the X-ray gas (i.e., 3C 249.1*a* and 4C 37.43*a* and *b*) are reminiscent of the classical picture of galactic superwinds. It has been shown

⁴ <http://heasarc.gsfc.nasa.gov/Tools/w3pimms.html>

in many edge-on starburst galaxies (*e.g.*, NGC 253, NGC 4945) that the X-ray gas shows a limb-brightened filamentary structure, and lies either coincident with, or just to the inside of, H α emission-line filaments (Cecil, Bland-Hawthorn, & Veilleux 2002; Strickland et al. 2004). The underlying mechanism is most likely either that (1) as the high-speed hot wind and the cold ISM intermingle, the dense ambient gas becomes entrained and heated in the wind fluid, resulting in both optical emission and local increases in the X-ray emissivity; or (2) as the superwind encounters a large cloud, it produces a slow (10^2 km s $^{-1}$) radiative shock into the cloud and a fast (10^3 km s $^{-1}$) stand-off bow shock; the former produces the optical emission, the latter the X-rays (Lehnert, Heckman, & Weaver 1999). Similarly, in a case where the extended X-ray emission does tend to follow the extended optical emission, this correlation may be due to thermal emission from shocks within the extended emission region, produced by superwinds associated with a recent interaction- or merger-driven starburst. These shocks would also provide a natural explanation for the higher-density regions found from modeling the optical emission-line spectrum.

If a galactic superwind due to a starburst is indeed the cause of the extended optical and X-ray emission around quasars, then there are at least two predictions that can be used to test the model: (1) There must be high-velocity shocks in the emission-line regions, and the thermal emission from these shocks may, in some regions, dominate the photoionization of the surrounding gas by UV radiation from the quasar nucleus; (2) The post-starburst ages of the host galaxies must be young, *i.e.*, on the order of tens of Myr or less. The time it takes for the high-speed wind gas to travel from the nucleus to the EELRs is less than a few tens of Myr, given a typical wind velocity of 10^3 km s $^{-1}$ and a typical EELR distance of a few tens of kpc from the center of the host galaxy.

In order to carry out the first test, two conditions must hold: (1) there must be regions where shocks are present but the gas is shielded from a direct line-of-sight to the nucleus, and (2) we must be able to distinguish the signature of ionization from shocks from that of photoionization by the quasar continuum. This latter requirement is complicated by the fact that much of the emission-line radiation from a high-velocity shock can be due to photoionization of the pre-shock gas by the thermal continuum from the shock itself. Such “autoionizing” shock models are distinguished from nuclear photoionization models by the shape of the ionizing-photon spectrum in the vicinity of the emission-line regions. There are intrinsic differences, with the nuclear continuum following an approximate power law over many decades in frequency, in contrast to the thermal spectrum of the shock. But the nuclear emission is also likely to be subject to higher photo-

electric absorption of soft X-rays due to intervening material, further increasing the relative hardness ratio of the ionizing radiation. These differences in the ionizing continuum are reflected in the ratios of certain diagnostic emission lines, and both of these forms of photoionization can be distinguished from each other and from pure shock ionization by their emission spectra (Villar-Martin, Tadhunter, & Clark 1997; Allen, Dopita, & Tsvetanov 1998). Unfortunately, the most useful strong lines tend to be in the ultraviolet region inaccessible from the ground for objects of modest redshift. However, with efficient spectrographs on large ground-based telescopes, it is now feasible to use weaker lines, such as [O III] λ 4363 and He II λ 4686. Evans et al. (1999) have shown that the [O III] λ 4363/[O III] λ 5007 vs. He II λ 4686/H β diagram could be a very powerful diagnostic for discriminating nuclear photoionization models and high-speed shock models (see their Fig. 10). Realistic nuclear photoionization models, shock photoionization models, and pure shock-ionized models are all reasonably well separated in this diagram.

We have so far been assuming that a global superwind can only be due to a starburst. However, another possibility is that the superwind could be a direct result of the turning on of the quasar itself (di Matteo, Springel, & Hernquist 2005). In this case, although the test for whether shock models can explain the line emission is still appropriate, we wouldn’t necessarily expect to see an extremely recent starburst.

Whatever the origin of the high-velocity gas, the detection of discrete X-ray features associated with two of our quasar fields seems clearly to point to the presence of high-speed shocks. This picture is consistent with evidence from extended optical emission, in particular, (1) the existence of small regions of dense gas that cannot be in hydrostatic pressure equilibrium with their surroundings, and (2) gas velocities that exceed those that can reasonably be attributed to gravitation. Given the lack of correlation of any of these features with radio jets, some sort of galactic wind seems the most reasonable possibility.

Support for this work was provided by the National Aeronautics and Space Administration (NASA) through Chandra Award Number GO3-4126 issued by the Chandra X-ray Observatory Center, which is operated by the Smithsonian Astrophysical Observatory for and on behalf of NASA under contract NAS8-03060. This research has also been partially supported by NSF grant AST03-07335. It made use of the NASA/IPAC Extragalactic Database (NED) which is operated by the Jet Propulsion Laboratory, California Institute of Technology, under contract with the National Aeronautics and Space Administration. The authors recognize the very significant cultural role that the summit of Mauna Kea has within the indigenous Hawaiian community and are grateful to have had the opportunity to conduct observations from it.

REFERENCES

- Allen, M. G., Dopita, M. A., & Tsvetanov, Z. I. 1998, *ApJ*, 493, 571
 Birkinshaw, M., & Worrall, D. M. 1993, *ApJ*, 412, 568
 Boroson, T. A., Persson, S. E. & Oke, J. B. 1985, *ApJ*, 293, 120
 Canalizo, G., & Stockton, A. 2000b, *AJ*, 120, 1750
 Carter, C. 2003, *ASP Conf. Ser.*, 295, 477
 Cavaliere, A., & Fusco-Femiano, R. 1978, *A&A*, 70, 677
 Cecil, G., Bland-Hawthorn, J., & Veilleux, S. 2002, *ApJ*, 576, 745
 Crawford, C. S., & Fabian, A. C. 1989, *MNRAS*, 239, 219
 Crawford, C. S., Fabian, A. C., & Johnstone, R. M. 1988, *MNRAS*, 235, 183
 Crawford, C. S., & Vnderriest, C. 2000, *MNRAS*, 315, 433
 di Matteo, T., Springel, V., & Hernquist, L. 2005, *Nature*, 433, 604
 Evans, I., Koratkar, A., Allen, M., Dopita, M., & Tsvetanov, Z. 1999, *ApJ*, 521, 531
 Fabian, A. C., Crawford, C. S., Johnstone, R. M., & Thomas, P. A. 1987, *MNRAS*, 228, 963
 Forbes, D. A., Fabian, A. C., Johnstone, R. M., & Crawford, C. S. 1990, *MNRAS*, 244, 680

- Kellermann, K. I., Sramek, R. A., Schmidt, M., Green, R. F., & Shaffer, D. B. 1994, *AJ*, 108, 1163
- Kinkhabwala, A., Sako, M., Behar, E., Kahn, S. M., Paerels, F., Brinkman, A. C., Kaastra, J. S., Gu, M. F., & Liedahl, D. A. 2002, *ApJ*, 575, 732
- Lehnert, M. D., Heckman, T. M., & Weaver, K. A. 1999, *ApJ*, 523, 575
- MacKenty, J. W., & Stockton, A. 1984, *ApJ*, 283, 64
- Marshall, H. L., Schwartz, D. A., Lovell, J. E. J., Murphy, D. W., Worrall, D. M., Birkinshaw, M., Gelbord, J. M., Perlman, E. S. Jauncey, D. L. 2005, *ApJS*, 156, 13
- Miller, P., Rawlings, S., & Saunders, R. 1993, *MNRAS*, 263, 425
- Mulchaey, J. S., & Zabludoff, A. I. 1998, *ApJ*, 496, 73
- Peterson, J. R. et al. 2003, *ApJ*, 590, 207
- Richstone, D. O., & Oke, J. B. 1977 *ApJ*, 213, 8
- Sako, M., Kahn, S. M., Paerels, F., & Liedahl, D. A. 2000, *ApJ*, 543, L115
- Sambruna, R. M., Gambill, J. K., Maraschi, L. Tavecchio, F., Cerutti, R. Cheung, C. C., Urry, C. M., & Chartas, G. 2004, *ApJ*, 608, 698
- Sanders, D. B., Scoville, N. Z., & Soifer, B. T. 1988, *ApJ*, 335, 1
- Stockton, A. 1976, *ApJ*, 205, L113
- Stockton, A., & MacKenty, J. W. 1983, *Nature*, 305, 678
- Stockton, A., & MacKenty, J. W. 1987, *ApJ*, 316, 584
- Stockton, A., MacKenty, J. W., Hu, E. M., & Kim, T.-S. 2002, *ApJ*, 572, 735
- Strickland, D. K., Heckman, T. M., Colbert, E. J. M., et al. 2004, *ApJ*, 606, 829
- Sutherland, R. S., & Dopita, M. A. 1993, *ApJS*, 88, 253
- Villar Martín, M., Tadhunter, C., & Clark, N. 1997, *A&A*, 323, 21
- Wampler, E. J., Robinson, L. B., Burbidge, E. M., & Baldwin, J. A. 1975, *ApJ*, 198, L52
- Young, A. J., Wilson, A. S., Terashima, Y., Arnaud, K. A., & Smith, D. A. 2002, *ApJ*, 564, 176